DOI: 10.1002/ ((please add manuscript number))

Article type: Full paper

Arrays of Planar Vacancies in Superior Thermoelectric $Ge_{1-x-y}Cd_xBi_yTe$ with Band Convergence

Min Hong, Yuan Wang, Weidi Liu, Syo Matsumura, Hao Wang, Jin Zou, and Zhi-Gang Chen

Dr. M. Hong, Y. Wang, Prof. H. Wang, Prof Z.-G. Chen

Centre for Future Materials, University of Southern Queensland, Springfield, Queensland 4300, Australia.

Email: zhigang.chen@usq.edu.au

Dr. M. Hong, W. Liu, Prof. J. Zou Prof Z.-G. Chen

Materials Engineering, University of Queensland, Brisbane, Queensland 4072, Australia.

Prof. S. Matsumura

Department of Applied Quantum Physics and Nuclear Engineering, Kyushu University, Motooka 744, Nishi-ku, Fukuoka 819-0395, Japan.

Prof. J. Zou

Centre for Microscopy and Microanalysis, University of Queensland, Brisbane, Queensland 4072, Australia.

Email: j.zou@uq.edu.au

Keywords: GeTe alloys, high-performance thermoelectrics, planar vacancies, TEM characterizations, band convergence

Abstract

The multi-valence bands in GeTe provide an additional handle to manipulate the thermoelectric performance. Herein, the density-functional-theory calculation indicates that Cd doping enables the convergence of these multi-valence bands. Plus, the additional Bi dopant serving as the electron donors optimizes the carrier concentration, leading to an enhanced power-factor in $Ge_{1-x-y}Cd_xBi_yTe$. Moreover, our comprehensive electron microscopy characterizations demonstrate the array of high-density planar vacancies in $Ge_{1-x-y}Cd_xBi_yTe$ stemming from the absence of {111} Ge atomic planes, which is driven by the reduced formation energy in the scenario of Cd/Bi co-doping. Simulations of phonon transport confirm the significant role of planar vacancies in scattering mid-frequency phonons. Such high-density planar vacancies, in tandem with grain boundaries and point defects, lead to a lattice thermal conductivity of 0.4 W $m^{-1}K^{-1}$ in $Ge_{1-x-y}Cd_xBi_yTe$, reaching the amorphous limit. Ultimately, a peak zT of 2.2 is realized, which promotes GeTe into the first echelon of cutting-edge thermoelectric materials. The strategy of combining band convergence and planar vacancies opens a revenue to develop Pb-free derivatives with super-high thermoelectric efficiency.

1. Introduction

The rising demand for green energy has sparked significant research into alternative energy sources and energy harvesting technologies. As one of the promising candidates, thermoelectricity enables the direct interconversion between heat and electricity.[1] Thermoelectric behavior is associated with three material parameters, including Seebeck coefficient (S), electrical conductivity (σ), and thermal conductivity (κ, consisting of electronic component κ_e and lattice component κ_l).[2] To quantify the energy conversion efficiency at a certain working temperature (T), the dimensionless figure-of-merit (zT) can be defined as $zT = S^2\sigma T/\kappa$.[3] Feasibility of thermoelectric materials is closely pertinent to the conversion efficiency, which eventually craves a large zT, involving the enhancement of power-factor ($S^2\sigma$) and the reduction of κ.

Carrier concentration (n), band structure, and microstructure are three key factors to impact thermoelectric properties for a given material. The interplay relationship of S, σ, and κ_e leads to an optimal n to compromise S and σ, and to counterbalance κ_e. Band structures significantly affect electronic transport *via* band degeneracy,[4] band effective mass,[5] and distortion of density-of-states (DOS) near the Fermi level (E_f).[6] Accordingly, enhanced thermoelectric performances have been witnessed in PbTe-,[7-9] SnTe-,[10-12] and Mg_2Sn-based materials[13-15] resulting from band convergence; in I-doped PbTe,[16] $Yb_xCo_4Sb_{12}$,[17] and Te-doped $Mg_3Sb_{1.5}Bi_{0.5}$[18] due to the decreased inertial effective mass; and in Tl-doped PbTe,[6,19] In-doped GeTe,[20,21] and In-doped SnTe[22,23] caused by resonant-dopant induced DOS distortion near E_f. Phonon propagation can be extrinsically impeded by scattering centers of grain boundaries, nanoprecipitates, dislocations, and point defects, which, respectively, account for the decreased κ_l in Bi_2Te_3-based nanostructures;[24-27] in SnTe[28-31] and PbSe;[32-34] in Bi_2Te_3-[25,35,36] and PbTe-based materials;[37,38] and alloyed/doped solid solutions.[39-42] Recently, as the interstitial dopant, Cu has successfully pushed κ_l close to the amorphous limit in SnTe-based materials.[11,43] In the amorphous structure, phonons are strongly scattered by disorder, and their lifetimes reach the minimum time scale of thermal vibrations.[44] The value in the amorphous structure with the same chemical composition is often considered as a lower bound for

the lattice thermal conductivity.[45] Therefore, revisiting the classical lattice imperfections for decreasing κ_l, together with enhanced $S^2\sigma$, may pave a way to develop next-generation thermoelectrics with super-high performance.

GeTe with the rhombohedral (R) – to – cubic (C) phase transition is a promising candidate to replace toxic PbTe for mass-market applications. Electrically, GeTe (particularly cubic phase) has multi-valence bands with high band degeneracy, ensuring a large $S^2\sigma$. Sb/Bi-doped GeTe was reported to show peak zT of ~1.7 through tuning n to the optimal level,[46,47] which rationalizes the superior band structures of GeTe for ensuring high electronic transport. Thermally, the naturally existed precipitates and Ge vacancies in GeTe-based alloys result in a decreased κ_l.[48,49] In fact, Ge vacancies mainly scatter high-frequency phonons, which overlap with the role of point defects originating from doping/alloying.[39] On the other hand, it is possible to form other scattering centers targeting on, for instance, mid-frequency phonons, evolving from the Ge vacancies, to further decrease κ_l.

In this study, motivated by the multi-valence bands of both R- and C-GeTe (shown in Figure 1a and b), we theoretically predict thermoelectric performance by engineering the two valence bands of GeTe. The details of three-band modeling of electronic transport can be seen in Section 1 of Supporting Information. Figure 1c plots calculated $S^2\sigma$ and zT as a function of reduced Fermi level (η) for both R- and C-GeTe at 300 K and 700 K using a three-band model of one conduction band (CB) and two valence bands (VBs) at L and Σ points. As can be seen, both $S^2\sigma$ and zT increase significantly especially at high temperature by converging these two VBs. The amorphous limit of κ_l for GeTe[50] is used to calculated zT. Note that cubic GeTe has intrinsically lower κ_l than rhombohedral GeTe, which is due to (i) the existence of cation lone pair s2 electrons in cubic GeTe leads to strong anharmonic phonon-phonon interactions and (ii) coordination number of cubic GeTe (six) doubles that of rhombohedral GeTe, resulting in lower phonon group velocity in cubic GeTe. Thereby, it would be more likely to decrease the practical κ_l of cubic GeTe to approach the amorphous limit. Experimentally, we employ Cd as the dopant to decrease the energy offset (ΔE) between the VBs, as predicted by the calculated band structures in $Ge_{1-x}Cd_xTe$. With the additional Bi doping to tune n, $S^2\sigma$ has been optimized in our $Ge_{1-x-y}Cd_xBi_yTe$. Moreover, arrays of a high-density of planar vacancies have been found in sintered pellets through our atomic-resolved electron microscopy characterization, as schematically illustrated in Figure 1d. Consequently, an ultra-low κ_l close to the amorphous limit has been realized in our $Ge_{1-x-y}Cd_xBi_yTe$. The enhanced $S^2\sigma$ and decreased κ_l lead to a peak zT of 2.2 in $Ge_{1-x-y}Cd_xBi_yTe$ (Figure 1e), which is higher than the reported values for the cutting-edge mid-temperature thermoelectric materials (Figure S1). The thermal stability of obtained high thermoelectric properties has been confirmed by the cycling measurements within three heating-cooling processes (refer to Figure S2).

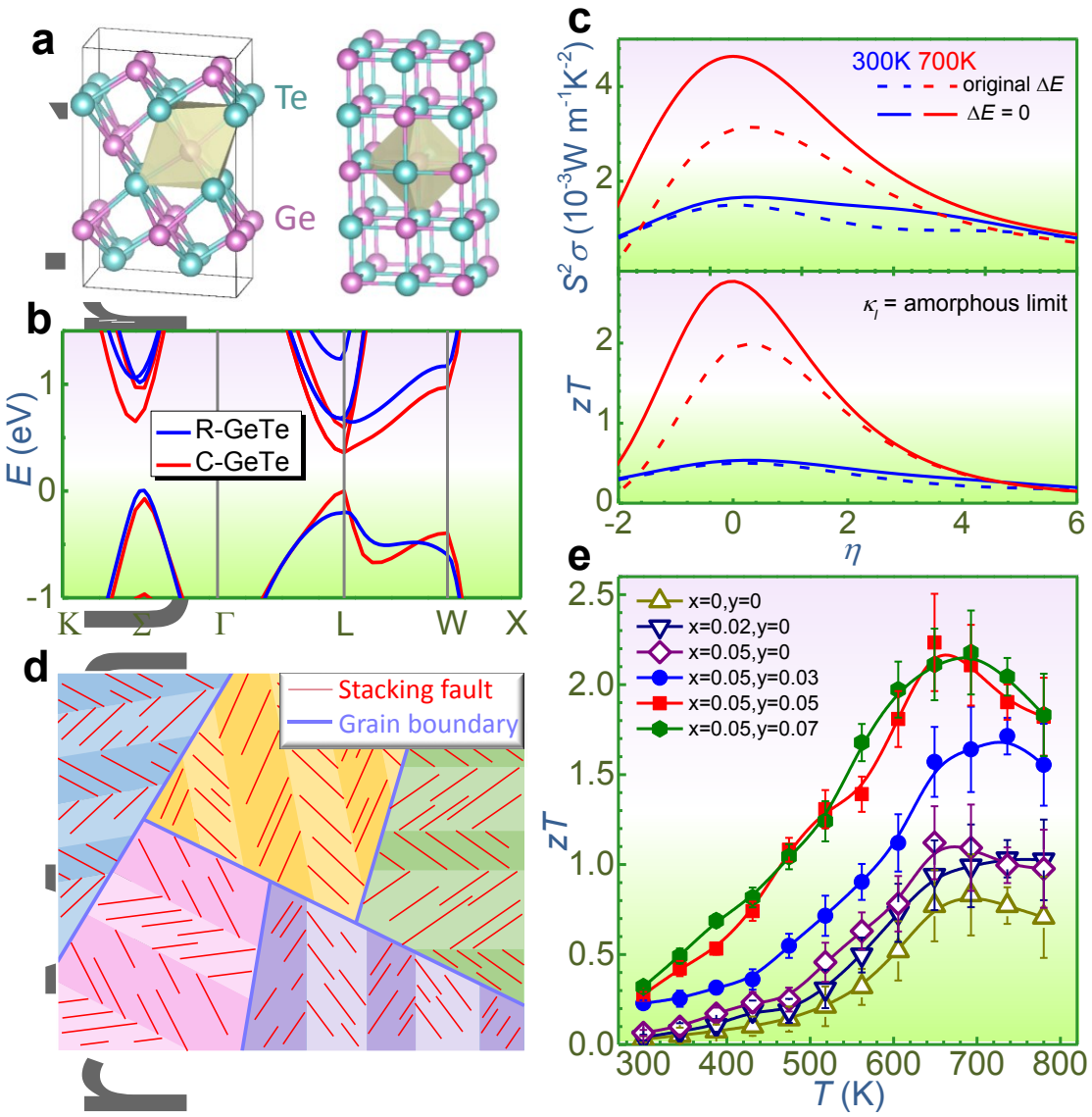

Figure 1 Strategies for enhancing the thermoelectric efficiency of GeTe-based materials. (a) Crystal structures and (b) calculated band structures for rhombohedral (R-) and cubic (C-) GeTe. (c) Calculated power factor ($S^2\sigma$) and figure of merit (zT) as a function of reduced Femi level (η) for both R- and C-GeTe at 300 K and 700 K using a three-band model of one conduction band and two valence bands at L and Σ points. Here, the amorphous limit of lattice thermal conductivity (κ_l) for GeTe is used to calculate zT. (d) Schematic diagram showing the array of a high-density of planar vacancies within grains to enhance phonon scatterings. (e) Measured temperature-dependent zT for $Ge_{1-x-y}Cd_xBi_yTe$.

2. Results and Discussion

2.1 Analysis of the Obtained Electronic Transport

The as-obtained powders without detectable impurities (refer to XRD patterns in Figure S3) are consolidated into pellets by spark plasma sintering (SPS) to evaluate their thermoelectric performance. The sintered pellet of $Ge_{0.88}Cd_{0.05}Bi_{0.07}Te$, as an example, are examined by energy-dispersive X-ray spectroscopy (EDS) mapping, as shown in Figure S4. Despite the Ge precipitates, the elements distributed evenly in the analyzed sample. Figure 2a shows the measured S as a function of

temperature for all $Ge_{1-x-y}Cd_xBi_yTe$. The positive sign of *S* indicates the *p*-type transport behavior with holes dominating the free charge carriers, and the magnitude of *S* increases with raising the content of Cd and the additional Bi. Specifically, the peak *S*, initializing at ~150 μV K^{-1} for the pristine GeTe, increases to ~170 μV K^{-1} in $Ge_{0.95}Cd_{0.05}Te$ and ends up with an even higher value of ~ 240 μV K^{-1} in $Ge_{0.88}Cd_{0.05}Bi_{0.07}Te$. Figure 2b shows the temperature-dependent σ, which decreases with increasing the doping content. The variation of both *S* and σ strongly relies on the Hall carrier concentration (n_H) and Hall carrier mobility (μ_H), depicted in Figure 2c and d, respectively. While Cd doping does not modify n_H notably, Bi can effectively tune the n_H in a wide range. Unfavorably, doping with Cd or Bi decreases μ_H to some extent. Moreover, the declining trend of μ_H upon temperature follows the power low of $T^{-0.16}$, suggesting acoustic phonons dominating the charge carrier scatterings.[51]

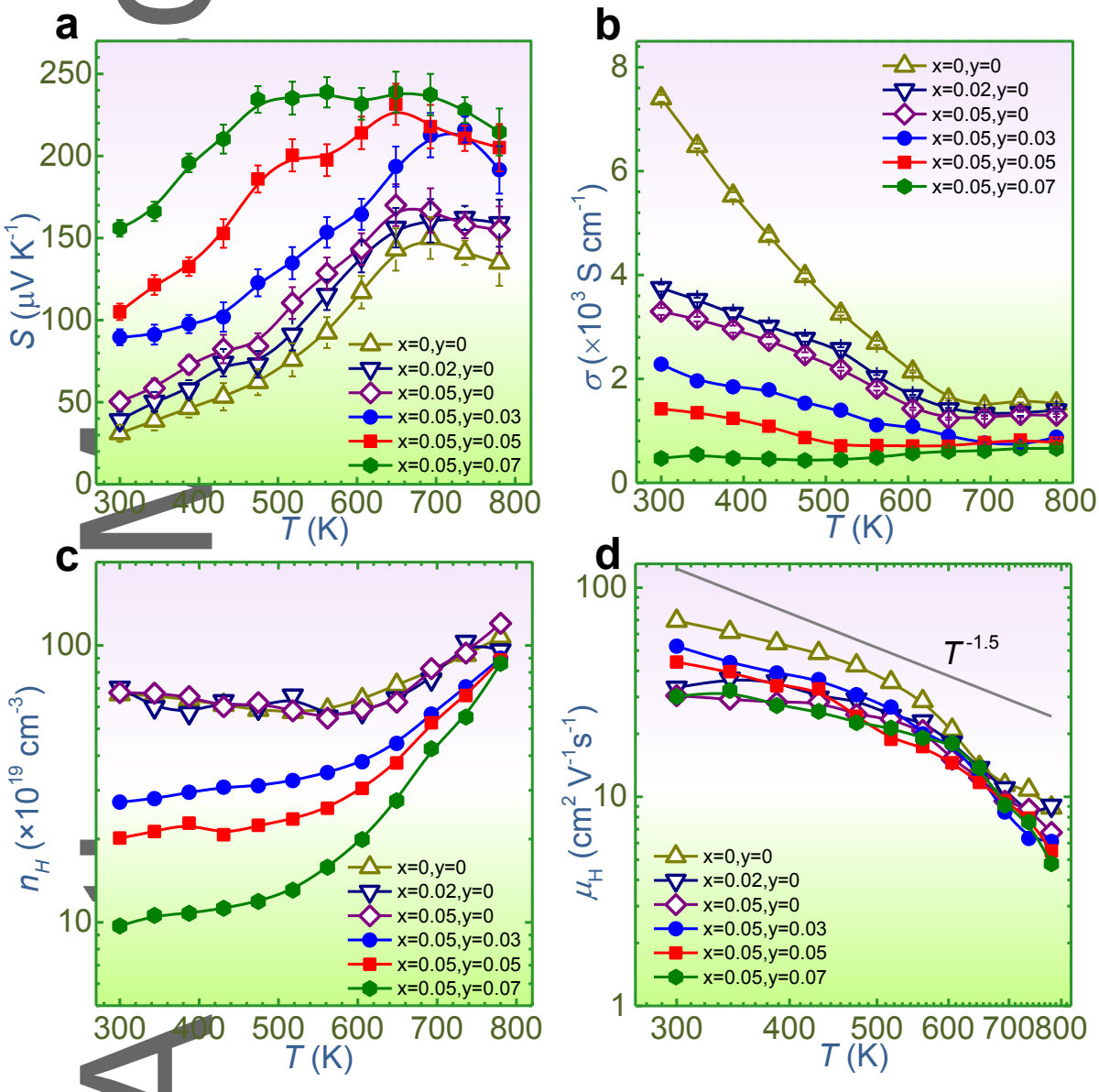

Figure 2 Electronic transport coefficients. Temperature-dependent (a) Seebeck coefficient (*S*), (b) electrical conductivity (σ), (c) Hall carrier concentration (n_H), and (d) Hall carrier mobility (μ_H) for $Ge_{1-x-y}Cd_xBi_yTe$.

To examine the electronic transport characteristics of our pellets, we calculate n_H-dependent S and n_H-dependent μ_H based on the single Kane band (SKB) model,[16] in which we assume that acoustic phonons dominate the scattering of charge carriers, confirmed by the measured μ_H following a power law of $T^{-1.5}$ (refer to Figure 2d). As described above, *p*-type GeTe has multi-valence bands affecting the electronic transport coefficients; therefore, the related physical parameters in the invoked SKB model, such as the DOS effective mass (m_d^*) can be regarded as the weighted sum of the corresponding tensor from each single band.[52]

Figure 3a shows the measured S values as a function of n_H at 300 and 700 K compared with the calculated plots of n_H-dependent S, in which the hollow data points correspond to $Ge_{1-x}Cd_xTe$ and the solid data points are from $Ge_{1-x}Cd_xBi_yTe$. Since the relationship of S *versus* n_H is predominantly affected by m_d^* in the SKB model, the upward trend of the S *versus* n_H curves for $Ge_{1-x}Cd_xTe$ with higher x serves as the diagnostic of the significantly varied m_d^* upon Cd doping at both 300 and 700 K. By contrast, with the role of tuning n_H in a wide range for GeTe, Bi-doping does not affect m_d^* notably, as evidenced by the generally gathered curves of S *versus* n_H for $Ge_{1-x}Cd_xBi_yTe$. Compared with the Ge (+2) ions, Cd has a valence of +2, while Bi has a valence of +3. Thereby, Bi serves as the electron donors to decrease the hole concentration in GeTe, whereas Cd doping does not modify hole concentration notably. Quantitatively, we determine the composition-dependent m_d^* at both 300 and 700 K by two steps. First, we derive η according to the measured S using Equation S1. Then, according to the Equation S2 with the measured n_H, we determine m_d^*. As shown in Figure 3b, doping especially with Cd can essentially increase m_d^*. Figure 3c shows the comparison of μ_H *versus* n_H plots with the experimental data points, in which μ_H degenerates in $Ge_{1-x-y}Cd_xBi_yTe$ with increasing the doping content, caused by the unfavorably strengthened charge carrier scatterings.[39] As for electronic transport coefficients, $S^2\sigma$ is the ultimate parameter to evaluate the overall thermoelectric efficiency. Figure 3d shows temperature-dependent $S^2\sigma$ for $Ge_{1-x-y}Cd_xBi_yTe$, from which $S^2\sigma$ is enhanced when co-doping with Cd and Bi. Specifically, a maximal $S^2\sigma$ = 40 $\mu Wcm^{-1}K^{-2}$ is achieved for the $Ge_{0.86}Cd_{0.08}Bi_{0.06}Te$ pellet. The enhanced $S^2\sigma$ can be ascribed to the enlarged m_d^* by Cd and decreased n_H to the optimal level by Bi. Enlarged m_d^* reflects the modified band structures due to Cd doping.[16]

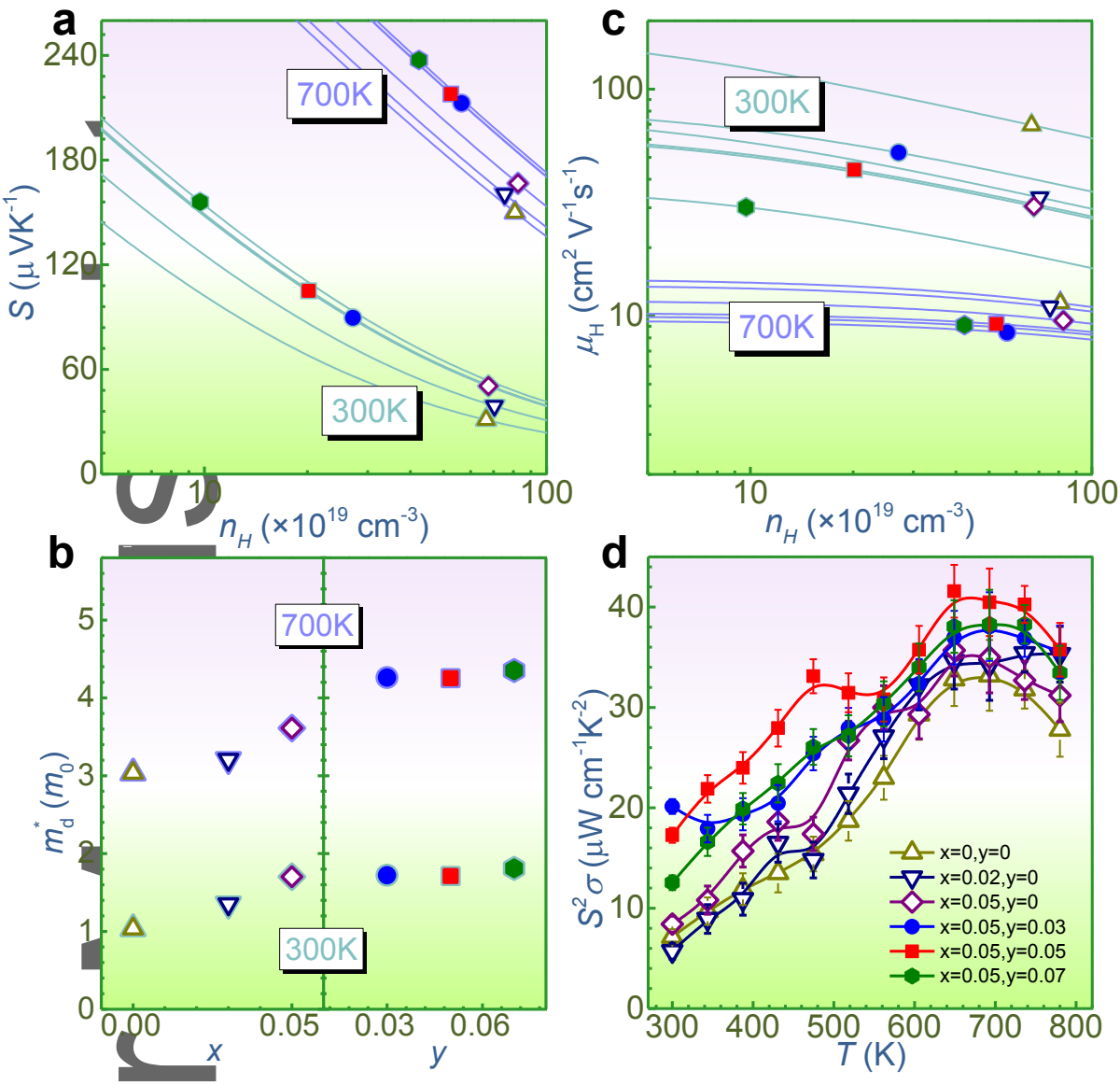

Figure 3 Analysis of electronic transport coefficients. (a) Calculated curves of Hall carrier concentration (n_H) dependent Seebeck coefficient (S) compared with the measured data points *versus* n_H at 300 K and 700 K; (b) calculated n_H-dependent Hall carrier mobility (μ_H) compared with the data points at 300 and 700 K; (c) determined density-of-states effective mass (m_d^*) for $Ge_{1-x-y}Cd_xBi_yTe$ with different compositions at 300 K and 700 K; and (d) temperature-dependent power factor ($S^2\sigma$).

2.2 Examination of Electronic Band Structures

To examine the doping effect on electronic band structures of GeTe, we perform the density-functional-theory (DFT) calculation with spin-orbital-coupling (SOC) for Cd-doped and pristine GeTe. Figure 4a and b display the calculated band structures for R-GeTe and C-GeTe, respectively. While the green curves denote the band structure for pristine GeTe, the red curves are the band structures for Cd-doped GeTe. With Ge sites partially replaced by Cd, both the indirect E_g (from L to Σ points of the first Brillouin zone) of R-GeTe and the direct E_g (at L point) of C-GeTe have been enlarged, which advantageously suppress the bipolar conduction. Since the electronegativity (χ) of Cd (χ = 1.69) is smaller than Ge (χ = 2.01)[53], the Cd-Te bond is weaker than Ge-Te bond, which is responsible for the enlarged E_g in Cd-doped GeTe.[3] Along with the enlarged E_g, the magnitude of lowered VB extrema

at L and Σ points is different, leading to the decreased Δ*E* for both R-GeTe and C-GeTe. Consequently, the contribution of secondary VB (*i.e.*, VB_L of R-GeTe and VB_Σ of C-GeTe) to the electronic transports has been magnified, which interprets the increase of the determined m_d^* from the SKB model upon Cd doping. Noteworthy, the Cd doping introduces an impurity band close to the CB edge, plotted as the purple dash curve in Figure 3a and b.

According to the total DOS and the decomposed partial density of states (PDOS) for R-GeTe and C-GeTe (Figure 4c and d), Ge_$4p^2$ orbitals dominate CB minimum and Te_$5p^4$ orbitals in conjunction with Ge_$4s^2$ orbitals govern VB maxima in both GeTe phases. In the doped scenario, Cd_$5s^2$ orbitals contribute to the impurity band, which could serve as the deep defect states (DDS).[54] Since the optimal n_H is found to increase with temperature by roughly following $(Tm_d^*)^{1.5}$,[55] the DDS induced by Cd_$5s^2$ orbitals might ensure a maximized $S^2\sigma$ by releasing holes for *p*-type $Ge_{1-x-y}Cd_xBi_yTe$ at high temperature.

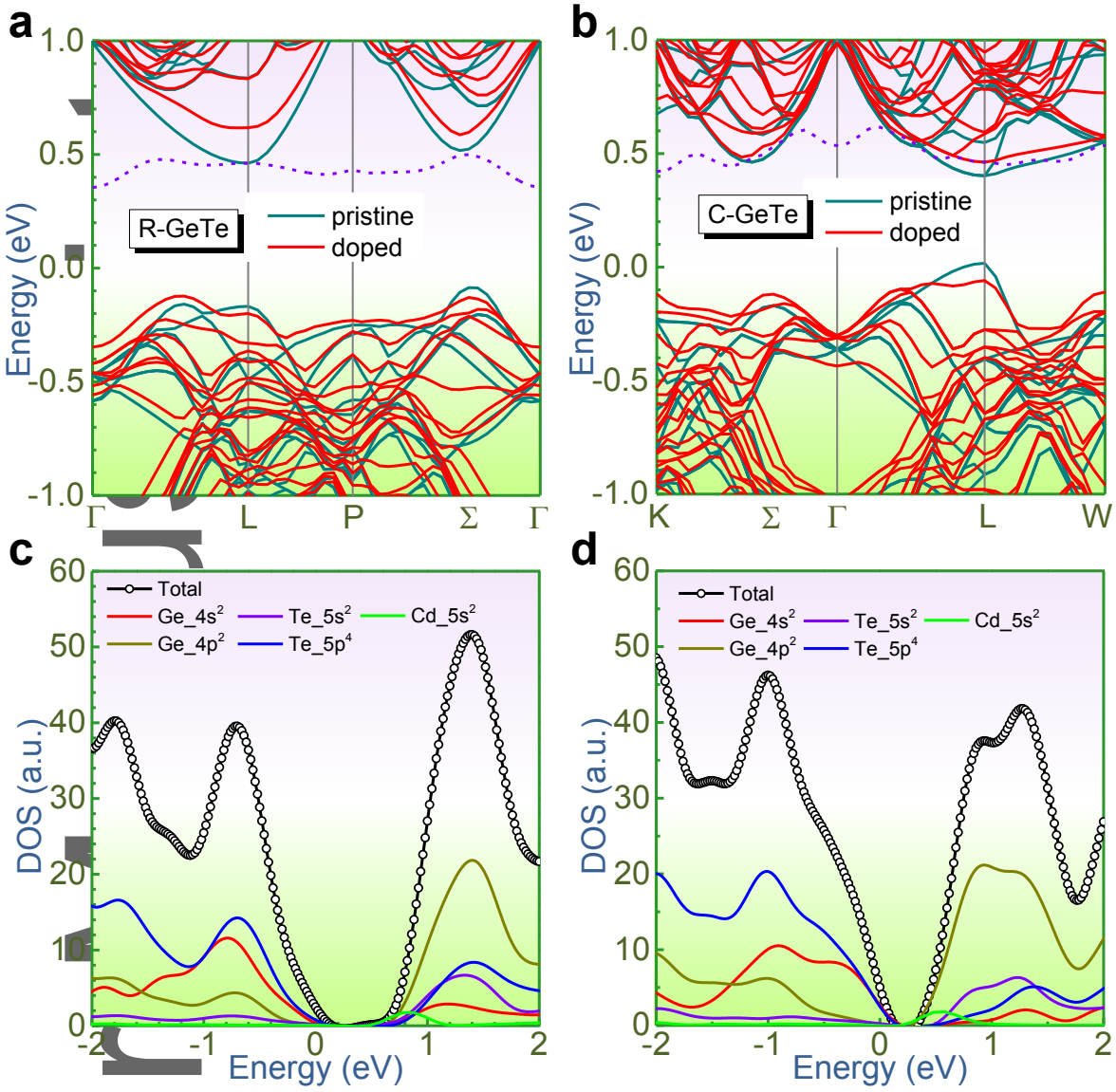

Figure 4 Effect of Cd-doping on the band structures. Calculated band structures for (a) rhombohedral (R-) and (b) cubic (C-) GeTe with SOC. The green and red curves correspond to the pristine and doping cases. Calculated density-of-states (DOS) for Cd-doped (c) R-GeTe and (d) C-GeTe.

2.3 Microstructure Characterizations

Since the microstructure of $Ge_{1-x-y}Cd_xBi_yTe$ can significantly affect phonon scatterings, which turns to decrease κ, detailed transmission electron microscopy (TEM) investigations were performed to understand the microstructures of our sintered $Ge_{1-x-y}Cd_xBi_yTe$ pellets. Figure 5a shows a TEM image taken from a typical grain in our sintered $Ge_{0.9}Cd_{0.05}Bi_{0.05}Te$ pellet, in which parallel domains with width ranging from 100 – 200 nm can be seen. Furthermore, each domain contains a high density of streaks. Figure 5b is an enlarged TEM image and shows the details of streaks — they are planar defects. The inset of Figure 5b is the corresponding selected area electron diffraction (SAED) pattern, from which the domain interfaces are found to be along [001] directions and the streaks are parallel

to {111} atomic planes. The formation of these domains is caused by the slight lattice distortion of {110} plans, which is confirmed by the split of high-index diffraction spots along the [110] directions in the inset of Figure 5b.

To understand the detailed atomic structure of the streaks, we employed aberration-corrected scanning TEM (STEM) to investigate their atomic configuration. Figure 5c shows a typical high angle annular dark field (HAADF) STEM image, in which several planar defects (marked by the red arrows) can be clearly seen. Figure 5d is an enlarged HAADF STEM image to present the detailed atomic structure of a typical planar defect. In HADDF STEM imaging mode, the intensity of atomic columns is roughly proportional to $Z^{1.7}$ with Z denoting the atomic number.[56] As a consequence, bright atomic columns are ascribed to heavier elements, which are Te with Z = 52, while the weak atomic columns are Ge with Z = 32. Figure 5e is the intensity profile of the marked atomic columns in Figure 5d, in which the high- and low-intensity peaks originate from bright (Te) and weak (Ge) atomic columns, respectively. Accordingly, the observed streaks/planar defects are due to the missing of a Ge atomic plane on the $\{111\}$ planes.

To understand the energetic origin of the observed planar vacancies, we perform the DFT calculation to determine their formation energies (E_{form}) in the pristine GeTe, with no dopants, with individual Cd, Bi dopant, and with Cd/Bi co-dopants. Figure 5f plots the calculated E_{form} as a function of the Fermi level (E_f) varying within the gap region in different circumstances, in which doping with Cd or Bi can decrease E_{form} and the Cd/Bi co-doping leads to the lowest E_{form}. Therefore, the formation of planar vacancies is energetically favorable in our case. It is well-known that there are large amounts of intrinsic Ge vacancies in GeTe.[57] The observed planar vacancies might evolve from the Ge vacancies associated with a decreased E_{form} in $Ge_{1-x-y}Cd_xBi_yTe$.[58]

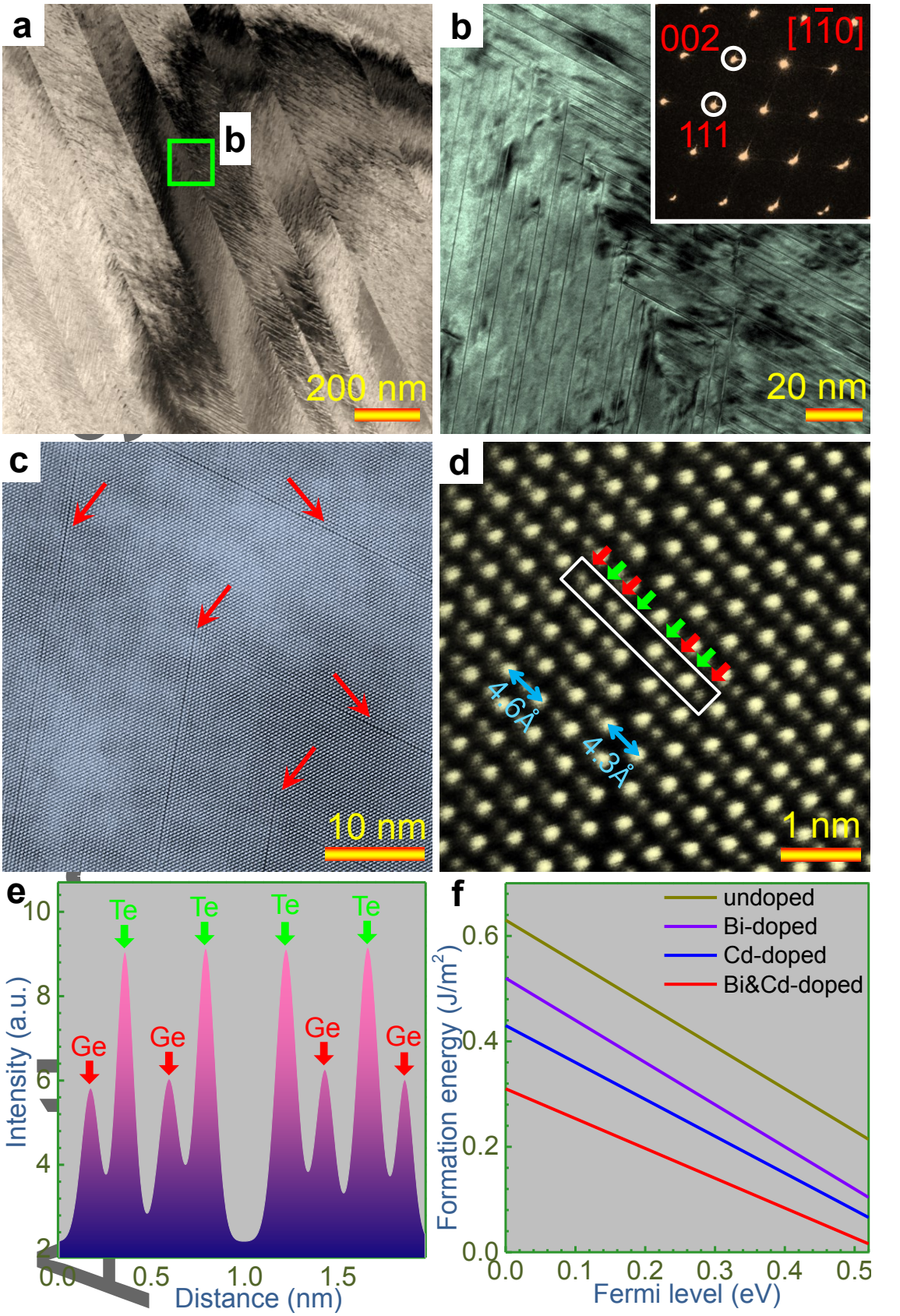

Figure 5 | Microstructure investigations of $Ge_{0.9}Cd_{0.05}Bi_{0.05}Te$. (a) Low-magnification transmission electron microscope (TEM) image, and (b) the enlarged view of the framed area in (a) with the inset showing the corresponding SAED

pattern. (c) High-angle annular dark-field (HAADF) scanning transmission electron microscopy (STEM) image taken from the marked area in (c) to show several planar vacancies. (d) Magnified HAADF STEM image showing the atomic configuration of a typical stacking fault. (e) Line profile showing the image intensity along the framed area in (d). (f) Formation energy of planar vacancies with different doping elements.

2.4 Analysis of Phonon Transport

Based on the above TEM characterizations, we further investigate the measured κ for $Ge_{1-x-y}Cd_xBi_yTe$. Figure 6a plots the measured κ as a function of temperature. With increasing the Cd doping content and additional Bi, κ continuously decreases over the entire temperature range. To examine the individual thermal components of electrons and phonons, we calculate κ_e according to the Wiedemann–Franz law (*i.e.*, $\kappa_e = L\sigma T$, with L representing the Lorenz number, shown in Figure S7a, Supporting Information), and then determine κ_l using $\kappa - \kappa_e$. Temperature-dependent κ_e is summarized in Figure S7b, and the variation of temperature-dependent κ_l is plotted in Figure 6b. As can be seen, κ_e decreases remarkably with increasing the doping content, making a partial contribution to the κ reduction. In addition, the considerably reduced κ_l leads to a further decrease in κ. Specifically, the lowest κ_l is ~ 0.4 W $m^{-1}K^{-1}$ in $Ge_{0.88}Cd_{0.05}Bi_{0.07}Te$, which reaches the amorphous limit of GeTe.[50] As uncovered by the comprehensive structural characterizations, the obtained ultra-low κ_l results from the co-existence of grain boundaries, nanoprecipitates (shown in Figure S8), point defects (stemming from the mass and size fluctuations between the dopants of Cd or Bi and the substituted Ge atoms in the lattice), and planar vacancies, which synergistically strengthen phonon scatterings.

To examine the individual role of these phonon scattering sources on decreasing κ_l, we numerically investigate the phonon transport using the Debye-Callaway model by taking into account different phonon scatterings of Umklapp processes (U), grain boundaries (B), nanoprecipitates (NP), point defects (PD), and planar vacancies (PV). Herein, we calculate the spectral lattice thermal conductivity (κ_s). Figure 6c shows the curves of κ_s as a function of phonon frequency (ω) by models of U, U+B, U+B+NP, U+B+NP+PD, and U+B+NP+PD+PV at 300 K. Because the integral of κ_s with respect to the phonon frequency equals the corresponding κ_l, the area between two adjacent curves is the decreased magnitude of κ_l caused by the introduction of the additional phonon scattering center. As can be seen, both B and NP are responsible for low-frequency phonon scatterings, while point defects target on high-frequency phonons. As a supplement, planar vacancies focus on mid-frequency phonons. Based on the Debye-Callaway model of U+B+NP+PD+PV, the calculated temperature-dependent κ_l can predict the experimental value of $Ge_{0.88}Cd_{0.05}Bi_{0.07}Te$, refer to Figure 6b. Figure 6d shows the comparison of our obtained lowest κ_l with the reported values for the state-of-arts GeTe-based counterparts. As can be seen, our obtained κ_l is relatively lower than the values of other GeTe family. Therefore, planar vacancies are a type of phonon scattering sources targeting on mid-frequency phonons to effectively decrease κ_l.

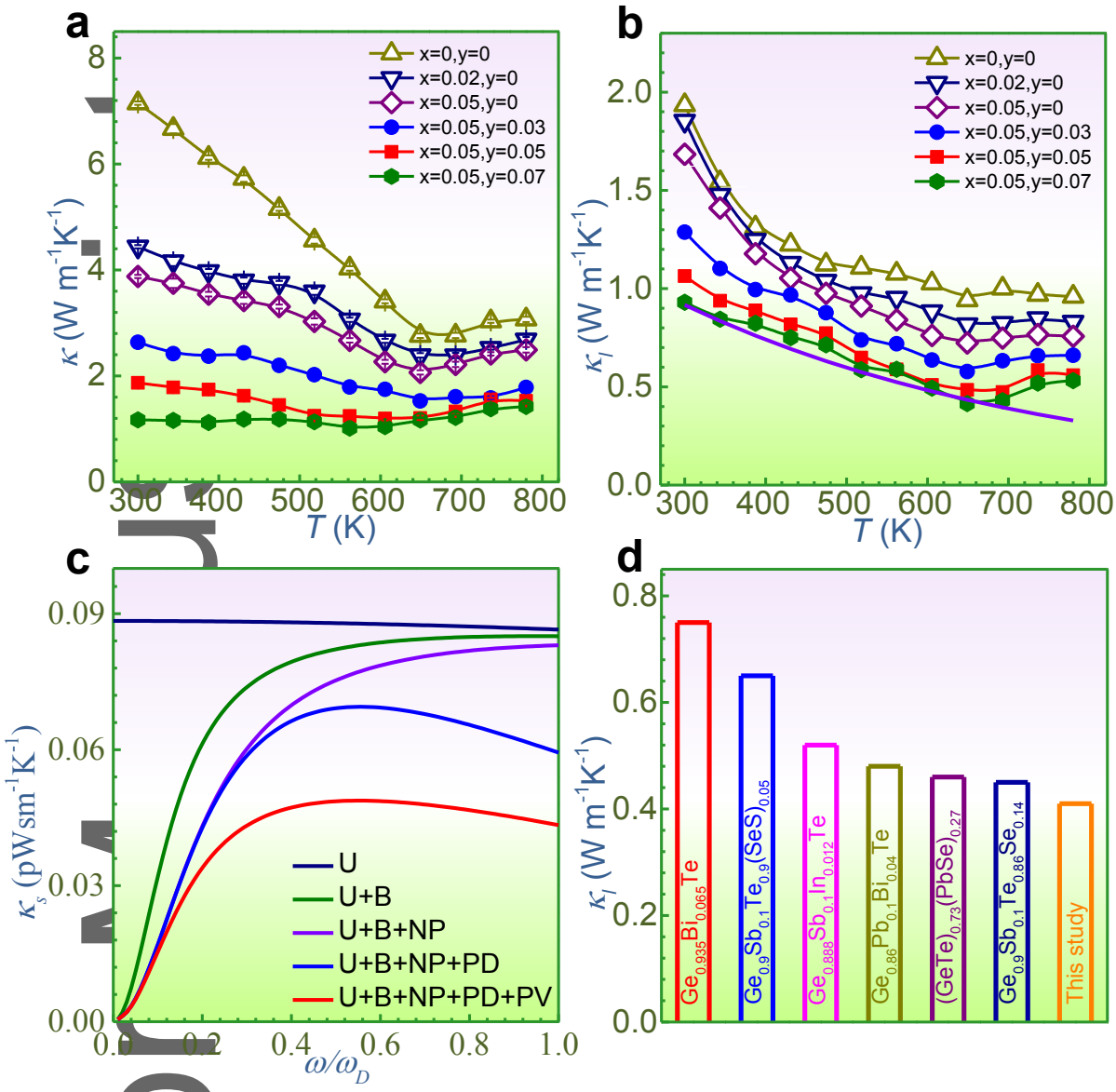

Figure 6 Analysis of thermal transport properties. Temperature-dependent (a) κ and (b) κ_l for $Ge_{1-x-y}Cd_xBi_yTe$ with different compositions. (c) Calculated κ_s using Debye-Callaway model with different phonon scatterings of Umklapp processes (U), grain boundaries (B), nanoprecipitates (NP), point defects (PD), and planar vacancies (PV) at 300 K. (d) Comparison of the lowest κ_l for $Ge_{0.88}Cd_{0.05}Bi_{0.07}Te$ with the reported values for $Ge_{0.935}Bi_{0.065}Te$,[46] $Ge_{0.9}Sb_{0.1}Te_{0.9}(SeS)_{0.05}$,[48] $Ge_{0.888}Sb_{0.1}In_{0.012}Te$,[21] $Ge_{0.86}Pb_{0.1}Bi_{0.04}Te$,[59] $(GeTe)_{0.73}(PbSe)_{0.27}$,[50] and $Ge_{0.9}Sb_{0.1}Te_{0.86}Se_{0.14}$.[47]

3 Conclusion

We synthesize a series of $Ge_{1-x-y}Cd_xBi_yTe$ ($x \le 0.05$, $x \le 0.07$) thermoelectric materials, delivering a super-high peak $zT > 2.0$ associated with the enhanced $S^2\sigma$ and the decreased κ. The calculated band structures reveal that Cd doping can efficiently decrease ΔE between the sub-valence bands of GeTe, which accounts for the enhanced $S^2\sigma$, provided that n_H is fully optimized by the additional Bi doping. The decreased κ can be attributed to the strongly enhanced phonon scatterings. The microstructural investigations using advanced electron microscopy demonstrates the existence of a high density of

planar vacancies in Cd/Bi co-doped GeTe, which is confirmed to be effective to scatter mid-frequency phonons by the simulation study of phonon transport using Debye-Callaway model. Therefore, planar vacancies in conjunction with the classical grain boundaries, nanoprecipitates, and point defects are responsible for the obtained ultra-low κ. The breakthrough of zT development in this study has lead GeTe to be a promising Pb-free candidate working near mid-temperature range, which provides a direction of exploring new-generation thermoelectric materials with zT beyond 2.0 by engineering band structures and introducing lattice imperfections.

4. Experimental Section

Material Synthesis: To synthesize $Ge_{1-x-y}Cd_xBi_yTe$, precursors of high-purity elemental Ge, Cd, Bi, and Te from Sigma-Aldrich were sealed in fused quartz tubes under vacuum. Quartz tubes were slowly heated to 950 ˚C, held for 6 hours, and followed by quenching in ice water. Samples were subsequently annealed at 650 ˚C for 3 days. The resulting ingots were ball-milled for 10 minutes into fine powders and consolidated by SPS under a pressure of 55 MPa at 550 ˚C for 5 min under vacuum. As shown in Table S1, densities of all sintered pellets were confirmed to be ~98 % of the theoretical density for GeTe by the Archimedes method.

Phase and Microstructure Characterization: The phase purities of as-sintered pellets were investigated by XRD, recorded on an X-ray diffractometer (Bruker D8 Advance MKII) equipped with graphite monochromatized, Cu $K\alpha$ radiation (λ = 1.5418 Å). The microstructure of the sintered pellets was investigated by scanning electron microscope (SEM, JEOL JSM-6610 equipped with Oxford 50mm2 X-Max SDD x-ray detector) and TEM (Philips Tecnai F20, and JEOL Arm200).

Thermoelectric Property Measurement: Thermal diffusivity (D) was measured by a laser flash method (LFA 457, NETZSCH, plotted in Figure S9), and κ was calculated using $\kappa = DC_pd$, where C_p and d are the specific heat capacity and density, respectively. C_P was determined using the Dulong-Petit law, which has been widely used in GeTe systems.[20,46-48] σ and S were measured simultaneously on a ZEM-3, ULVAC. The Hall coefficient (R_H) was measured using the Van der Pauw method in a magnetic field up to ±1.5T.[60] n_H and μ_H were respectively calculated using $n_H = 1/(eR_H)$ and $\mu_H = \sigma R_H$ with e representing the electron charge.

Density-Functional-Theory Calculation: DFT calculation was performed using the plane-wave self-consistent field (PWSCF) code as implemented in the QUANTUM-ESPRESSO suite of programs.[61] The exchange and correlation interactions were described using the local density approximation (LDA).[62] Values of 40 and 640 Ry were chosen as the cut-offs for the selection of the plane-wave basis sets for describing the kinetic energy and the electronic density, respectively. Spin-orbit coupling was included in the calculation. Supercell of 3×3×3 built from the primitive cell was used to calculate the band structures with a uniform mesh of 3×3×3 k-points, respectively. To examine the effect of doping on band structures, two Ge sites were randomly replaced by Cd. The structures were fully relaxed until the force on each atom was less than 10^{-5} eV Å^{-1}. Supercell of 6×6×3 built from the primitive cell was used to calculate E_{form} of planar vacancies with a uniform mesh of 2×2×3 k-points. E_{form} was calculated by $E_{form} = E_{tot}(\text{defects}) - E_{tot}(\text{host}) - \Sigma n_i u_i + qE_f$, in which E_{tot}(defects) and E_{tot}(host) are the total energies of supercells with and without planar vacancies, respectively.[63] n_i is the number of type i atoms that have been added to ($n_i > 0$) or removed from ($n_i < 0$) the supercell when the defect is created, and u_i is the corresponding chemical potential.[64] q is the charge on the defect

and E_f is the Fermi level. u_i for Ge, Cd, and Bi is determined by calculating the total energy of face-centered cubic Ge, hexagonal Cd, and monoclinic Bi, respectively.

Supporting Information

Supporting Information is available from the Wiley Online Library or from the author.

Acknowledgments

This work is financially supported by the Australian Research Council, the USQ start-up grant, the KU's Progress 100 program to encourage the UQ-KU collaboration, as well as the Nanotechnology Platform Project for advanced nanostructure characterization. The Australian Microscopy & Microanalysis Research Facility is acknowledged for providing characterization facilities. The Research Computing Centre at UQ is acknowledged for providing the computation clusters.

Received: ((will be filled in by the editorial staff))

Revised: ((will be filled in by the editorial staff))

Published online: ((will be filled in by the editorial staff))

References

[1] G. J. Snyder, E. S. Toberer, *Nat. Mater.* **2008**, *7*, 105.

[2] T. Zhu, Y. Liu, C. Fu, J. P. Heremans, J. G. Snyder, X. Zhao, *Adv. Mater.* **2017**, *29*, 1605884.

[3] W. G. Zeier, A. Zevalkink, Z. M. Gibbs, G. Hautier, M. G. Kanatzidis, G. J. Snyder, *Angew. Chem. Int. Edit.* **2016**, *55*, 6826.

[4] M. Hong, Z.-G. Chen, Y. Pei, L. Yang, J. Zou, *Phys. Rev. B* **2016**, *94*, 161201.

[5] Y. Pei, H. Wang, G. J. Snyder, *Adv. Mater.* **2012**, *24*, 6125.

[6] J. P. Heremans, B. Wiendlocha, A. M. Chamoire, *Energy Environ. Sci.* **2012**, *5*, 5510.

[7] Y. Pei, X. Shi, A. LaLonde, H. Wang, L. Chen, G. J. Snyder, *Nature* **2011**, *473*, 66.

[8] Z. Chen, Z. Jian, W. Li, Y. Chang, B. Ge, R. Hanus, J. Yang, Y. Chen, M. Huang, G. J. Snyder, Y. Pei, *Adv. Mater.* **2017**, *29*, 1606768.

[9] G. Tan, F. Shi, S. Hao, L.-D. Zhao, H. Chi, X. Zhang, C. Uher, C. Wolverton, V. P. Dravid, M. G. Kanatzidis, *Nat Commun* **2016**, *7*.

[10] G. Tan, F. Shi, S. Hao, H. Chi, T. P. Bailey, L.-D. Zhao, C. Uher, C. Wolverton, V. P. Dravid, M. G. Kanatzidis, *J. Am. Chem. Soc.* **2015**, *137*, 11507.

[11] W. Li, L. Zheng, B. Ge, S. Lin, X. Zhang, Z. Chen, Y. Chang, Y. Pei, *Adv. Mater.* **2017**, *29*, 1605887.

[12] A. Banik, U. S. Shenoy, S. Anand, U. V. Waghmare, K. Biswas, *Chem. Mater.* **2015**, *27*, 581.

[13] W. Liu, J. Zhou, Q. Jie, Y. Li, H. S. Kim, J. Bao, G. Chen, Z. Ren, *Energy Environ. Sci.* **2015**, *9*, 530.

[14] W. Liu, X. Tan, K. Yin, H. Liu, X. Tang, J. Shi, Q. Zhang, C. Uher, *Phys. Rev. Lett.* **2012**, *108*, 166601.

[15] X. Liu, T. Zhu, H. Wang, L. Hu, H. Xie, G. Jiang, G. J. Snyder, X. Zhao, *Adv. Energy Mater.* **2013**, *3*, 1238.

[16] Y. Pei, A. D. LaLonde, H. Wang, G. J. Snyder, *Energy Environ. Sci.* **2012**, *5*, 7963.

[17] Y. Tang, Z. M. Gibbs, L. A. Agapito, G. Li, H.-S. Kim, M. B. Nardelli, S. Curtarolo, G. J. Snyder, *Nat. Mater.* **2015**, *14*, 1223.

[18] J. Zhang, L. Song, S. H. Pedersen, H. Yin, L. T. Hung, B. B. Iversen, *Nat. Commun.* **2017**, *8*, 13901.

[19] J. P. Heremans, V. Jovovic, E. S. Toberer, A. Saramat, K. Kurosaki, A. Charoenphakdee, S. Yamanaka, G. J. Snyder, *Science* **2008**, *321*, 554.

[20] L. Wu, X. Li, S. Wang, T. Zhang, J. Yang, W. Zhang, L. Chen, J. Yang, *NPG Asia Mater.* **2017**, *9*, e343.

[21] M. Hong, Z.-G. Chen, L. Yang, Y.-C. Zou, M. S. Dargusch, H. Wang, J. Zou, *Adv. Mater.* **2018**, *30*, 1705942.

[22] Q. Zhang, B. Liao, Y. Lan, K. Lukas, W. Liu, K. Esfarjani, C. Opeil, D. Broido, G. Chen, Z. Ren, *Proc. Natl. Acad. Sci. USA* **2013**, *110*, 13261.

[23] G. Tan, F. Shi, S. Hao, H. Chi, L.-D. Zhao, C. Uher, C. Wolverton, V. P. Dravid, M. G. Kanatzidis, *J. Am. Chem. Soc.* **2015**, *137*, 5100.

[24] M. Hong, Z.-G. Chen, L. Yang, J. Zou, *Nanoscale* **2016**, *8*, 8681.

[25] M. Hong, T. C. Chasapis, Z.-G. Chen, L. Yang, M. G. Kanatzidis, G. J. Snyder, J. Zou, *ACS Nano* **2016**, *10*, 4719.

[26] M. Hong, Z. G. Chen, L. Yang, J. Zou, *Nano Energy* **2016**, *20*, 144.

[27] L. Yang, Z.-G. Chen, M. S. Dargusch, J. Zou, *Adv. Energy Mater.* **2018**, *8*, 1701797

[28] G. Tan, L.-D. Zhao, F. Shi, J. W. Doak, S.-H. Lo, H. Sun, C. Wolverton, V. P. Dravid, C. Uher, M. G. Kanatzidis, *J. Am. Chem. Soc.* **2014**, *136*, 7006.

[29] L.-D. Zhao, X. Zhang, H. Wu, G. Tan, Y. Pei, Y. Xiao, C. Chang, D. Wu, H. Chi, L. Zheng, S. Gong, C. Uher, J. He, M. G. Kanatzidis, *J. Am. Chem. Soc.* **2016**, *138*, 2366.

[30] H. Wu, C. Chang, D. Feng, Y. Xiao, X. Zhang, Y. Pei, L. Zheng, D. Wu, S. Gong, Y. Chen, J. He, M. G. Kanatzidis, L.-D. Zhao, *Energy Environ. Sci.* **2015**, *8*, 3298.

[31] R. Moshwan, L. Yang, J. Zou, Z.-G. Chen, *Adv. Funct. Mater.* **2017**, *27*, 1703278.

[32] K. Biswas, J. He, I. D. Blum, C. I. Wu, T. P. Hogan, D. N. Seidman, V. P. Dravid, M. G. Kanatzidis, *Nature* **2012**, *489*, 414.

[33] L.-D. Zhao, V. P. Dravid, M. G. Kanatzidis, *Energy Environ. Sci.* **2014**, *7*, 251.

[34] Y. Lee, S.-H. Lo, C. Chen, H. Sun, D.-Y. Chung, T. C. Chasapis, C. Uher, V. P. Dravid, M. G. Kanatzidis, *Nat. Commun.* **2014**, *5*, 4640.

[35] L. Hu, H. Wu, T. Zhu, C. Fu, J. He, P. Ying, X. Zhao, *Adv. Energy Mater.* **2015**, *5*, 1500411.

[36] S. I. Kim, K. H. Lee, H. A. Mun, H. S. Kim, S. W. Hwang, J. W. Roh, D. J. Yang, W. H. Shin, X. S. Li, Y. H. Lee, G. J. Snyder, S. W. Kim, *Science* **2015**, *348*, 109.

[37] Z. Chen, B. Ge, W. Li, S. Lin, J. Shen, Y. Chang, R. Hanus, G. J. Snyder, Y. Pei, *Nat. Commun.* **2017**, *8*, 13828.

[38] H. J. Wu, L. D. Zhao, F. S. Zheng, D. Wu, Y. L. Pei, X. Tong, M. G. Kanatzidis, J. Q. He, *Nat. Commun.* **2014**, *5*, 4515.

[39] H. Wang, A. D. LaLonde, Y. Pei, G. J. Snyder, *Adv. Funct. Mater.* **2013**, *23*, 1586.

[40] H. Wang, J. Wang, X. Cao, G. J. Snyder, *J. Mater. Chem. A* **2014**, *2*, 3169.

[41] G. Tan, L.-D. Zhao, M. G. Kanatzidis, *Chem. Rev.* **2016**, *116*, 12123.

[42] Z.-G. Chen, X. Shi, L.-D. Zhao, J. Zou, *Prog. Mater. Sci.* **2018**, *97*, 283.

[43] Y. Pei, L. Zheng, W. Li, S. Lin, Z. Chen, Y. Wang, X. Xu, H. Yu, Y. Chen, B. Ge, *Adv. Electron. Mater.* **2016**, *2*, 1600019.

[44] D. G. Cahill, S. K. Watson, R. O. Pohl, *Phys. Rev. B* **1992**, *46*, 6131.

[45] H. Mizuno, S. Mossa, J.-L. Barrat, *Sci. Rep.* **2015**, *5*, 14116.

[46] J. Li, Z. Chen, X. Zhang, Y. Sun, J. Yang, Y. Pei, *NPG Asia Mater.* **2017**, *9*, e353.

[47] J. Li, X. Zhang, S. Lin, Z. Chen, Y. Pei, *Chem. Mater.* **2016**, *29*, 605.

[48] M. Samanta, K. Biswas, *J. Am. Chem. Soc.* **2017**, *139*, 9382.

[49] D. Wu, L. Zhao, S. Hao, Q. Jiang, F. Zheng, J. W. Doak, H. Wu, H. Chi, Y. Gelbstein, C. Uher, C. Wolverton, M. Kanatzidis, J. He, *J. Am. Chem. Soc.* **2014**, *136*, 11412.

[50] J. Li, Z. Chen, X. Zhang, H. Yu, Z. Wu, H. Xie, Y. Chen, Y. Pei, *Adv. Sci.* **2017**, *4*, n/a.

[51] M. Hong, Z.-G. Chen, J. Zou, *Chin. Phys. B* **2018**, *27*, 048403.

[52] M. Hong, Z.-G. Chen, L. Yang, Z.-M. Liao, Y.-C. Zou, Y.-H. Chen, S. Matsumura, J. Zou, *Adv. Energy Mater.* **2018**, *8*, 1702333.

[53] G. A. Slack, in *CRC Handbook of Thermoelectrics*, (Ed: D. M. Rowe), CRC Press, Boca Raton, FL **1995**, 407.

[54] S. Ahmad, K. Hoang, S. D. Mahanti, *Phys. Rev. Lett.* **2006**, *96*, 056403.

[55] Y. Pei, Z. M. Gibbs, B. Balke, W. G. Zeier, G. J. Snyder, *Adv. Energy Mater.* **2014**, *4*, 1400486.

[56] Z. Wang, M. Saito, K. P. McKenna, L. Gu, S. Tsukimoto, A. L. Shluger, Y. Ikuhara, *Nature* **2011**, *479*, 380.

[57] D. H. Damon, M. S. Lubell, R. Mazelsky, *J. Phys. Chem. Solids* **1967**, *28*, 520.

[58] B. Yang, B. Liu, Y. Wang, H. Zhuang, Q. Liu, F. Yuan, X. Jiang, *Nanoscale* **2015**, *7*, 16237.

[59] J. Li, X. Zhang, Z. Chen, S. Lin, W. Li, J. Shen, I. T. Witting, A. Faghaninia, Y. Chen, A. Jain, L. Chen, G. J. Snyder, Y. Pei, *Joule* **2018**, *2*, 976.

[60] K. A. Borup, E. S. Toberer, L. D. Zoltan, G. Nakatsukasa, M. Errico, J.-P. Fleurial, B. B. Iversen, G. J. Snyder, *Rev. Sci. Instrum.* **2012**, *83*, 123902.

[61] P. Giannozzi, S. Baroni, N. Bonini, M. Calandra, R. Car, C. Cavazzoni, D. Ceresoli, G. L. Chiarotti, M. Cococcioni, I. Dabo, A. D. Corso, S. d. Gironcoli, S. Fabris, G. Fratesi, R. Gebauer, U. Gerstmann, C. Gougoussis, A. Kokalj, M. Lazzeri, L. Martin-Samos, N. Marzari, F. Mauri, R. Mazzarello, S. Paolini, A. Pasquarello, L. Paulatto, C. Sbraccia, S. Scandolo, G. Sclauzero, A. P. Seitsonen, A. Smogunov, P. Umari, R. M. Wentzcovitch, *J. Phys. Condens. Matter.* **2009**, *21*, 395502.

[62] J. P. Perdew, K. Burke, M. Ernzerhof, *Phys. Rev. Lett.* **1996**, *77*, 3865.

[63] C. G. V. d. Walle, J. Neugebauer, *J. Appl. Phys.* **2004**, *95*, 3851.

[64] N. Wang, D. West, J. Liu, J. Li, Q. Yan, B.-L. Gu, S. B. Zhang, W. Duan, *Phys. Rev. B* **2014**, *89*, 045142.

The table of contents entry

Band convergence and high-density planar vacancies render a figure-of-merit of 2.2 in $Ge_{0.9}Cd_{0.05}Bi_{0.05}Te$. Doping with Cd reduces the energy separation between the multi-valence bands in GeTe, which enhances the power-factor, provided the optimized carrier concentration by auxiliary Bi doping. Driven by the decreased formation energy, high-dense planar vacancies are formed in Cd/Bi co-doped GeTe, leading to an ultra-low thermal conductivity.

Keyword

GeTe alloys, high-performance thermoelectrics, planar vacancies, TEM characterizations, band convergence

Author

Min Hong, Yuan Wang, Weidi Liu, Syo Matsumura, Hao Wang, Jin Zou, and Zhi-Gang Chen

Title

Arrays of planar vacancies in superior thermoelectric $Ge_{1-x-y}Cd_xBi_yTe$ with band convergence

ToC figure